THE UNIVERSITY OF TEXAS AT DALLAS
McDermott Library

TREASURES
@UT Dallas

School of Natural Sciences and Mathematics
William B. Hanson Center for Space Sciences

Temporal Characteristic of the Mesoscale Plasma Flow Perturbations in the High-Latitude Ionosphere

UT Dallas Author(s):

Yun-Ju Chen
Roderick A. Heelis

Rights:

©2018 American Geophysical Union. All rights reserved.

Citation:

Chen, Yun-Ju, and Roderick A. Heelis. 2019. "Temporal Characteristic of the Mesoscale Plasma Flow Perturbations in the High-Latitude Ionosphere." Journal of Geophysical Research: Space Physics 124(1): 459-469, doi: 10.1029/2018JA026128

This document is being made freely available by the Eugene McDermott Library of the University of Texas at Dallas with permission of the copyright owner. All rights are reserved under United States copyright law unless specified otherwise.

JGR Space Physics

RESEARCH ARTICLE
10.1029/2018JA026128

Temporal Characteristic of the Mesoscale Plasma Flow Perturbations in the High-Latitude Ionosphere

Yun-Ju Chen[1] and **Roderick A. Heelis**[1]

[1]William B. Hanson Center for Space Sciences, University of Texas at Dallas, Richardson, TX, USA

Key Points:
- Residence time is longer for larger scale size flow perturbations in a fixed volume
- The growth times for all scale size are shorter than decay times
- A weak dependency on geomagnetic activity is seen but no dependency on IMF B_z

Correspondence to:
Y.-J. Chen and R. A. Heelis,
yxc126130@utdallas.edu;
heelis@utdallas.edu

Citation:
Chen, Y.-J., & Heelis, R. A. (2019). Temporal characteristic of the mesoscale plasma flow perturbations in the high-latitude ionosphere. *Journal of Geophysical Research: Space Physics*, *124*, 459–469. https://doi.org/10.1029/2018JA026128

Received 24 SEP 2018
Accepted 22 NOV 2018
Accepted article online 17 DEC 2018
Published online 3 JAN 2019

©2018. American Geophysical Union. All Rights Reserved.

Abstract Spatial and temporal characteristics of flow perturbations in the high-latitude ionosphere are important considerations for energy deposition from the magnetosphere. In this study, we examine the temporal characteristics of plasma flow perturbations with spatial scales between 100 and 400 km from two consecutive Defense Meteorological Satellite Program (DMSP) passes that have about the same orbital plane and sample time spacing between a few seconds and 20 min during local summer seasons in 2007-2015. The temporal characteristics of mesoscale flow perturbations are described by rise and saturation times for growth and decay derived from the changes in magnitude of perturbations and the time separation between consecutive samples. Observations suggest that the rise times for both growth and decay are shorter for small spatial scales (1–2 min, 100–200 km) and longer for large spatial scales (3–5 min, 200–400 km). The saturation time for decay is ~10 min for small scales and ~20 min for large scales. The growth saturation time is about 5–10 min for both scale sizes. These characteristic times for growth are always shorter than the decay times. If the difference in these characteristic times between growth and decay is produced by motion of a perturbation with the background flow through the observed volume, then a longitudinal scale size of 750 km or 1.5 hr of local time is implied.

1. Introduction

The high-latitude plasma convection pattern has been intensively studied for years utilizing satellite and radar observations that describe a large-scale (>1,000 km) view of the convection pattern and its dependency on season, dipole tilt, and different states in the solar wind (Pettigrew et al., 2010; Rich & Hairston, 1994; Ruohoniemi & Greenwald, 1996, 2005). In addition, empirical models of the convection pattern have been developed, which are responsive to a range of conditions in the solar wind (Cousins & Shepherd, 2010; Weimer, 2001). Analytical expressions for the electric potential configuration at high latitudes have also been constructed (Hairston & Heelis, 1990; Heelis et al., 1982). However, a significant amount of structure in the plasma motion or electric potential with gradient scale lengths of 500 km and less is present in the observation and is not captured by these statistical descriptions and models. These mesoscale features in electric potential or drift velocity superimposed on the large-scale convection pattern can contribute additional energy to the ionosphere and thermosphere in the form of Joule heating.

Joule heating and particle precipitation at high latitudes are two major heat sources from the magnetosphere that can perturb both the ionosphere and neutral atmosphere (Vickrey et al., 1982). The joule heating rate is usually given as a product of Pederson conductivity and electric field in the neutral rest frame, which has been shown to be equivalent to the total frictional heating rate dependent on ion mass density, the ion-neutral collision frequency, and relative ion-neutral velocity (St.-Maurice & Schunk, 1981; Vasyliunas & Song, 2005). The largest joule heating rate occurs in the *E* region where the Pederson conductivity is the largest. However, the most significant increases in the ion temperature are related to large electric fields in the *F* region (Heelis & Coley, 1988; Killeen et al., 1984).

Codrescu et al. (1995) illustrated an inconsistency in the location of the extremes in the neutral temperature between the coupled thermosphere-ionosphere mode (CTIM) (Fuller-Rowell et al., 1996) and Mass Spectrometer Incoherent Scatter (MSIS) neutral atmosphere model (Hedin, 1987) and attributed this inconsistency to the missing energy input from Joule heating due to the variability in electric field or drift velocity. Since then many studies have been carried out to characterize both the spatial and temporal variability in electric field from ground and space-based observations of the ion drift or electric field (Codrescu et al., 2000; Cousins & Shepherd, 2012; Johnson & Heelis, 2005; Matsuo et al., 2003; Matsuo & Richmond, 2008). It has been found that the intensity and spatial distribution of the variability with scale sizes less than

500 km depends on season, interplanetary magnetic field (IMF), gradient in the background ion drift, and location in magnetic latitude and local time. This variability has also been shown to be responsible for increases in the neutral temperature and result in significant changes in neutral density (Deng et al., 2009).

The temporal characteristics of the electric field variability have been examined by using EOF analysis applied to Super Dual Auroral Radar Network (SuperDARN) observations (Cousins et al., 2013). It was found that variability in the electric field with the smallest spatial scales and shortest time scales has a weaker dependency on the IMF orientation than the larger scale size and longer time scale variability. Other studies of the field-aligned current (FAC) density and particle precipitation used two consecutive satellites, one followed by another, to study the time scale of coherent features (Boudouridis & Spence, 2007; Gjerloev et al., 2011). A similar time scale, on the order of a few minutes, was found in current structure and particle precipitation structure with scale sizes between 100 and 1,000 km. On the dayside, coherent current structures are seen at shorter time separations between the satellites than that on the nightside. This was attributed to the different reconfiguration times of the magnetosphere on the dayside and nightside. A dependency of the temporal characteristics of FACs on IMF B_z and geomagnetic activity was seen on the nightside (Gjerloev et al., 2011).

Both the spatial and temporal variability in the electric field are important considerations for determining the joule dissipation in the ionosphere because this extra heating is dependent on the magnitude of the electric field variability and the time over which it is present in the system. Here we present a systematic study identifying mesoscale flow features with scale sizes between 100 and 400 km in the ion drift measurements from two consecutive passes taken from DMSP satellites. Our interest is to investigate the temporal persistence of these flow features and their dependence on the spatial scale size, orientation of the IMF, and geomagnetic activity. We found that flow features with smaller spatial scales generally have shorter residence times than the larger scale sizes. This characteristic time of the mesoscale features is found to be independent on IMF B_z but weakly dependent on geomagnetic activity.

2. Observations

Data from Defense Meteorological Satellite Program (DMSP) F13, F15, F16, F17, and F18 spacecraft are used in this study. Each satellite has an approximately Sun-synchronous orbit at altitude ~840 km and has an ion drift meter that provides the cross-track ion drift velocity in the direction perpendicular to the satellite track every 4 s (F13 and F15) or 1 s (F16, F17, and F18). Thus, the spatial size resolved by the sample cadence is about 70 or 20 km. During several periods from 2007 to 2015, two satellites have approximately the same orbital plane in magnetic coordinates with local time separation less than 0.5 hr and time spacings ranging from a few seconds to 20 min. This data set enables us to investigate the variability in flow features in a relatively small volume, as a function of the time separation between the satellites. We only consider the local summer months of May to August in the northern hemisphere and the months of November to February in the southern hemisphere since under these conditions the O^+ density is high and a high fidelity signal is obtained from the ion drift meter.

To investigate any relationship between the temporal characteristic of flow features and external drivers, the IMF measurements and auroral electrojet index (AE index) are used in this study. IMF data are propagated in time by 10 min to correspond to the time at the high-latitude ionosphere (Hairston & Heelis, 1995; Yu & Ridley, 2009). The AE index is used to indicate the geomagnetic activity in the auroral region. These data are available at the Space Physics Data Facility OMNIWeb interface.

3. Approach

In order to study the temporal characteristics of the mesoscale flow features in the high-latitude ionosphere, a first step is identifying those flow features in the underlying large-scale convection pattern. Figure 1 is an example event taken from DMSP F13 and F15 during a northern hemisphere pass on 16 August 2008. F13 crosses the pole around 15:07:07 UT and is followed by F15 ~1 min later. Two satellites have approximately the same orbital plane along the dawn-dusk meridian as shown in the polar diagram. The original cross-track drift velocity is shown in the top panel with F13 in black and F15 in red. Since the spatial size that can be resolved by the sample cadence of the instrument is about 70 km, we first apply a low-pass box-car

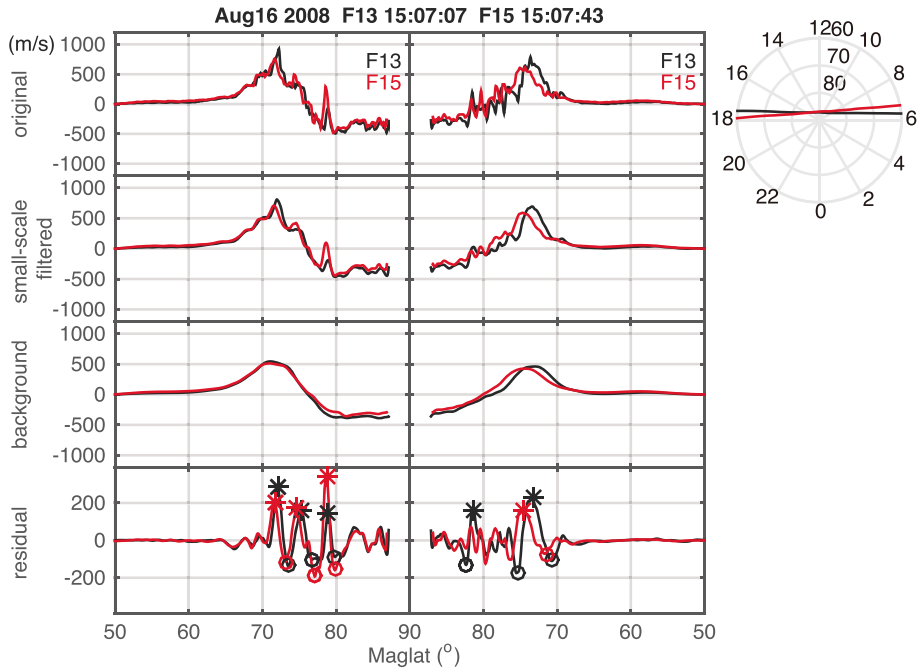

Figure 1. (first panel) Original cross-track drift velocity, (second panel) small-scale filtered drift velocity, (third panel) larger scale background convection, and (fourth panel) the residual drift velocity from the first encounter, F13 (black), and second encounter, F15 (red), are plotted as a function of magnetic latitude. Satellite orbits of F13 (black) and F15 (red) in magnetic latitude and local time are shown in the polar diagram.

filter to attenuate structures with scale sizes less than 100 km (second panel). We then identify a signature of the large-scale convection by attenuating all features with scale sizes less than 600 km utilizing a box-car average filter as shown in the third panel. Deviations from the large-scale background are obtained by subtracting the small-scale filtered ion drift measurement (second panel) from the large-scale convective flow signature (third panel). This residual velocity (bottom panel) shows the flow structures with scales between 100 and 600 km. Focusing on these isolated flow structures, we finally apply a wavelet analysis to this residual velocity from each pass to identify the spatial scale size of flow features and their location in magnetic latitude and local time.

Figure 2 is an illustration of the wavelet analysis. The first derivative of a Gaussian function is used as the wavelet to describe the shape of the flow structures (dotted blue lines in the top panel). Scale size is defined as the full width at half max of the peak of the Gaussian function (vertical dashed lines), which is approximately a half period of the wavelet. By changing the full width at half maximum, we are able to specify a wavelet with different width to represent a flow feature with different spatial scale size. In the middle panel, the black curve represents a sample feature shown in the time series flow data. We then perform the running inner product between the sample feature and wavelets with different scale sizes, to produce a map of the inner product as a function of scale size and time (bottom panel). The location of the local maxima in this map (red asterisk) indicates the trailing edge of the feature and the scale size that best describes the feature. We then find the positive (or negative) extrema in the velocity of the identified flow feature that is designated as a sunward directed (or antisunward directed) flow perturbation with respect to the large-scale background convection flow. The identified features for the example event are shown in the bottom panel of Figure 1 as circles and asterisks to denote the antisunward directed and sunward directed flow perturbations respectively. We apply the procedure described above on each pass to find the scale size, the location in magnetic latitude and magnetic local time, and also the peak velocity of each flow perturbation.

The same flow perturbations from consecutive passes are identified by the similarity in scale size and location of the flow perturbations. We allow the scale size to change by 25% and the location to change by 1.5° in magnetic latitude to account for a variability in the spatial size of the perturbations and the

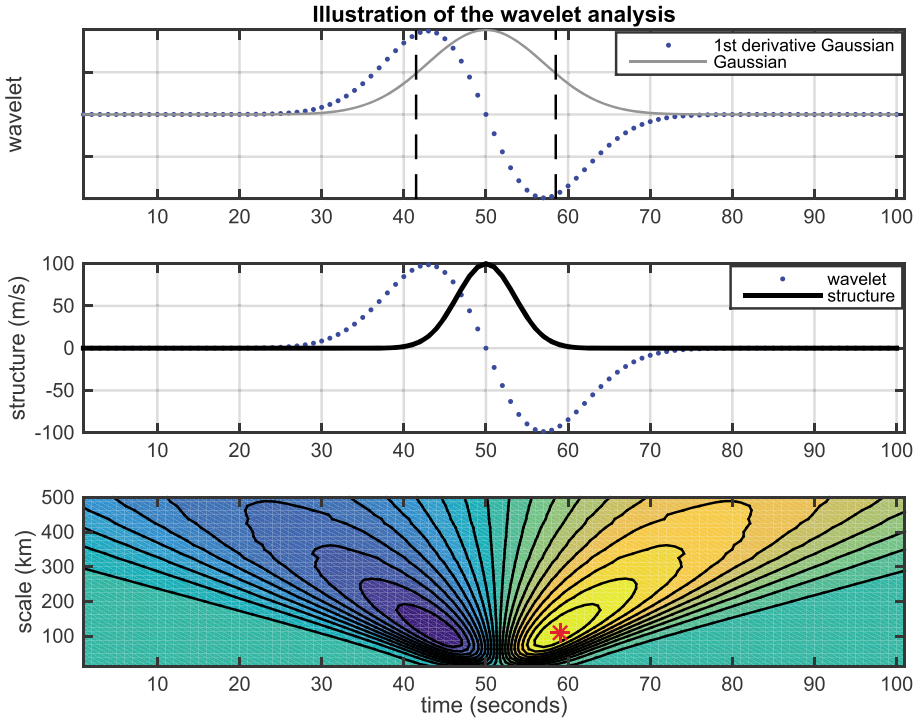

Figure 2. Illustration of feature identification by using the wavelet analysis. The blue dotted line represents the wavelet, and (top panel) the vertical dashed lines indicate the width (scale size) of the wavelet. (middle panel) A test data with one positive excursion shows in black solid line. (bottom panel) A two-dimensional map of the inner products between the wavelet with different width and the test data are plotted as function of time and scale size. The location of the local maximum (asterisk) is the result of this analysis indicating the feature location and spatial scale size.

movement of the perturbations due to expansion and contraction of the large-scale convection pattern. A percentage change (Pc) in the peak velocity of the flow perturbations observed by two consecutive passes is calculated to determine the growth or decay. We also require that the peak velocity of at least one of the flow perturbations observed by two encounters be larger than 100 m/s. Flow perturbations that are observed in only one pass are designated as appearing or disappearing with Pc of 100%. The time difference between first and second encounter of flow perturbations and the change in magnitude of the perturbations provides a time constant for growth, decay, appearance, or disappearance.

To investigate a dependency on the IMF and geomagnetic activity, each pair of flow perturbations captured by the two consecutive satellites is tagged with a median value of IMF and AE index over the time between the two encounters. Based on the median value of IMF and AE index, the observations are further divided into different groups: northward ($B_z > 0$) and southward IMF ($B_z < 0$) groups and disturbed (AE > 100) and quiet (AE < 100) groups. We note that our purpose is to compare the temporal characteristic of flow perturbations under different geomagnetic activity conditions, so the choice of the 100 nT threshold is driven by the need for sufficient statistics in each category.

4. Results

We collected a total of 3,378 consecutive passes from any combinations of measurements from the F13, F15, F16, F17, and F18 satellite taken between 2007 and 2015 in both hemispheres. The local time separation between the consecutive passes is less than 0.5 hr, and the universal time separation is less than 20 min. Figure 3 shows the numbers of consecutive passes (blue histogram) and the numbers of flow perturbations observed by the first satellite (red histogram) and second satellite (black histogram) as a function of the time separation between the two (Δt). More than 50% of the consecutive passes have a time spacing less than 4 min, and thus, large numbers of perturbations are identified in that time separation region. The numbers of flow perturbations observed by the first satellite are approximately the same as the numbers observed by

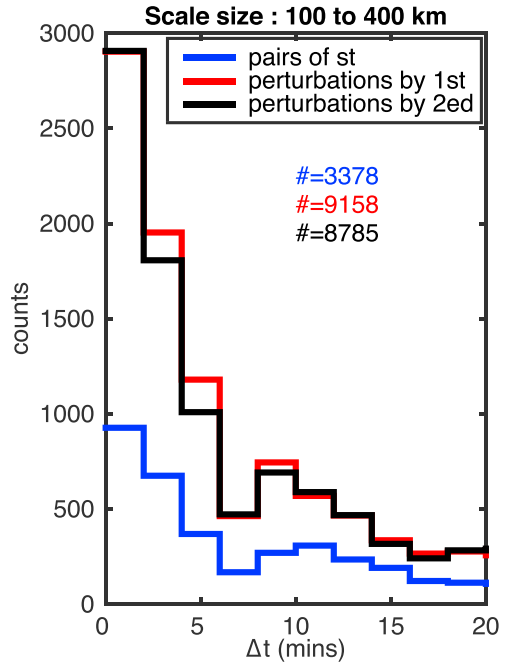

Figure 3. The numbers of consecutive passes (blue), flow perturbations observed by first satellite (red), and flow perturbations observed by the second satellite (black) are plotted as a function of the sampling time spacing.

the second satellite, which implies that mesoscale perturbations are commonly present in the high-latitude region at all times. We found that the sample size of perturbations with scale sizes between 400 and 600 km is quite small, and thus, we only consider scale sizes up to 400 km.

The locations of the flow perturbations in magnetic coordinates observed by the first (left) and second (right) satellite are shown in Figure 4. The coverage in local time is limited to the dusk and dawn sectors due to the configuration of the DMSP satellite orbits. There is no satellite in the noon-midnight meridian during the years of 2007 through 2015. Thus, the DMSP data are not sufficient to investigate the temporal characteristic of flow perturbations in the local noon and midnight regions. With the coverage around the dawnside and duskside, the perturbations are located in the auroral zone and polar cap region, but there are fewer flow perturbations at really high latitudes (above 85°). Note that we include the identified perturbations under all IMF orientations and magnetic activity levels and will discuss the dependence of the temporal characteristic of the perturbations on the IMF B_z and geomagnetic activity in a later section. In addition, the data used in this study cover only summer seasons and thus we will not examine the seasonal dependency of the characteristic time.

We first separate the identified perturbations into two groups based on the scale size: 100 to 200 km and 200 to 400 km and two groups based on the Pc in the magnitude of the perturbations, indicating growth or decay. To describe the temporal characteristics of the flow perturbations, we consider those perturbations that have grown or decayed by more than 50%. Figure 5 shows the histograms of all decaying perturbations (left) and decaying perturbations with changes greater than 50% (middle) as a function of the separation time between passes. Smaller scale sizes (100–200 km) are in the top panels, and larger scales (200–400 km) are in the bottom panels. Note that the sample numbers for different time separations are nonuniform. Thus, the right-side panels show the percentage of the perturbations decaying by more than 50% in each 2-min time separation bin. We then define a rise time as the shortest separation time at which more than 60% of these features are observed and a saturation time as the shortest separation time at which more than 80% of these features are observed. The right-side panels show that nearly 60% of the smaller scale perturbations that have decayed by more 50% are observed after 2 min and 60% of the larger scale perturbations that have decayed by more than 50% are observed after 5 min. Thus, the rise time for decay is about 2 min and 5 min for small and large scales, respectively. The time at which more than 80% of perturbations that have decayed more than 50% are observed is ~10 and >20 min for small and large spatial scales, respectively. We note that both the rise time and saturation time for decaying features are shorter for smaller scale sizes.

Figure 6 shows the histograms of all growing perturbations (left) and growing perturbations with changes more than 50% (middle) for smaller scale sizes on the top and larger scales on the bottom. As discussed above due to the nonuniform distribution of the samplings, in the right-side panels we show the fraction of growing perturbations with more than 50% changes in magnitude as a function of the time separation. In this case, as before, the rise time is shorter for the smaller scales (less than 2 min) than for the larger scales (~3 min). However, the saturation time is approximately the same (~5–10 min) for both smaller and larger scales.

In summary, we confined our consideration to those flow perturbations that are seen to grow or decay in magnitude by 50% or more. For these perturbations we find that growth times are shorter than decay times for both scale sizes and that rise times for both growth and decay are shorter for smaller scales. The granularity with which we can observe the saturation time at which more than 80% of the growing perturbations are observed is insufficient to accurately distinguish a difference for different scale sizes.

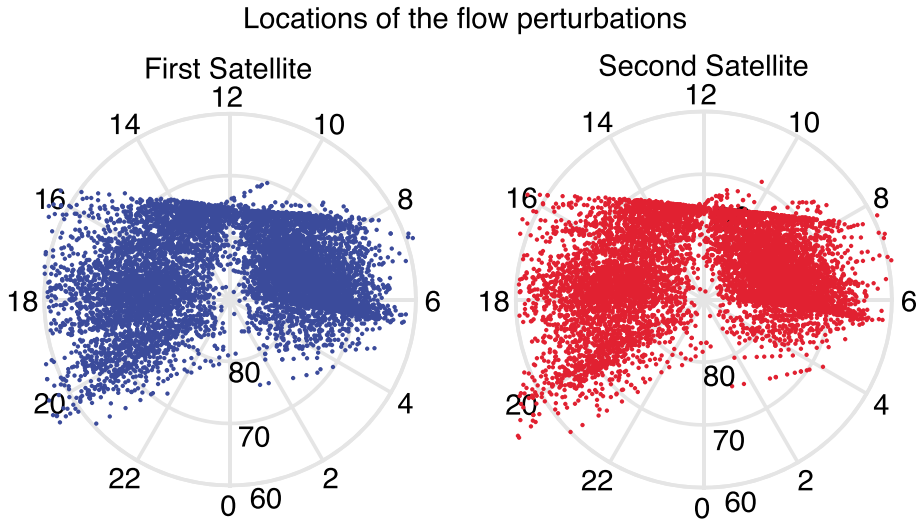

Figure 4. Location of the flow perturbations observed by (left) first and (right) second satellite in magnetic coordinate.

We further investigate the dependence of decaying and growing flow perturbations on magnetic activity. Figure 7 shows, as a function of time separation, the numbers of decaying perturbations (left), the numbers of perturbations that decay more than 50% in magnitude (middle), and the percentage of perturbations that decay more than 50% in magnitude (right) for disturbed times (AE $>$ 100, red) and quiet times (AE $<$ 100, black). For both smaller and larger scale perturbations, a higher fraction of perturbations that decay more than 50% is seen for disturbed times than quiet times (right panels). If we also choose an 80% threshold, the time separation at which smaller spatial scale perturbations are seen to decay more than 50% in

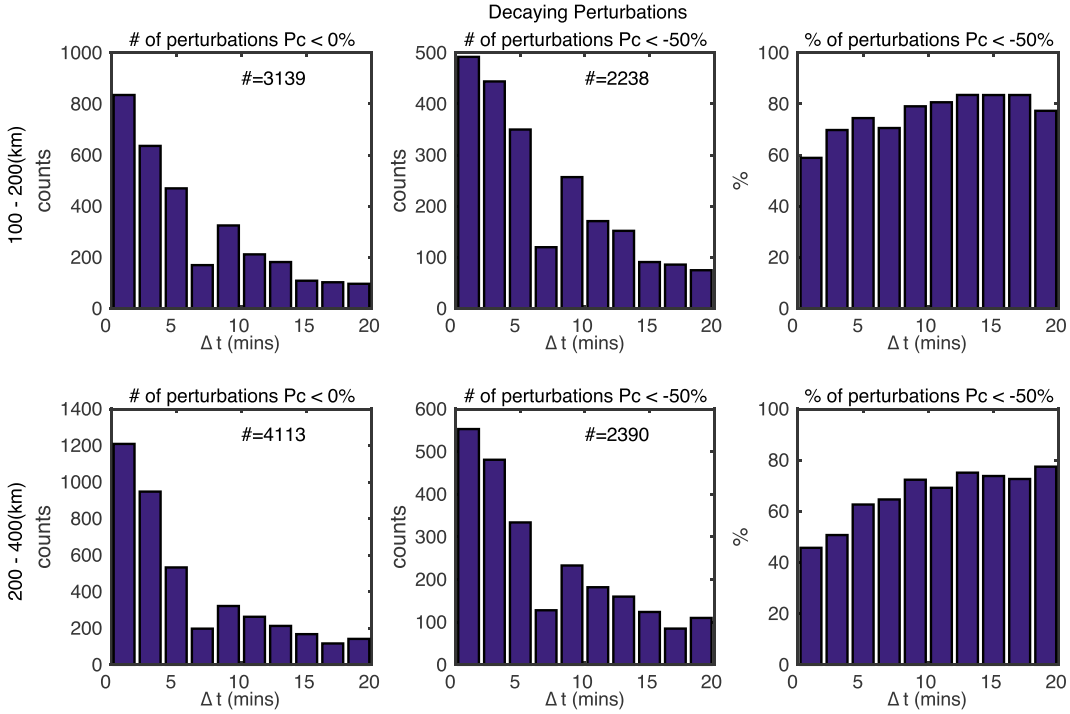

Figure 5. (left) The numbers of all decaying perturbations, (middle) decaying perturbations with more than 50% changes in magnitude, and (right) the percentage of the decaying perturbations with more than 50% changes in magnitude as a function of time difference.

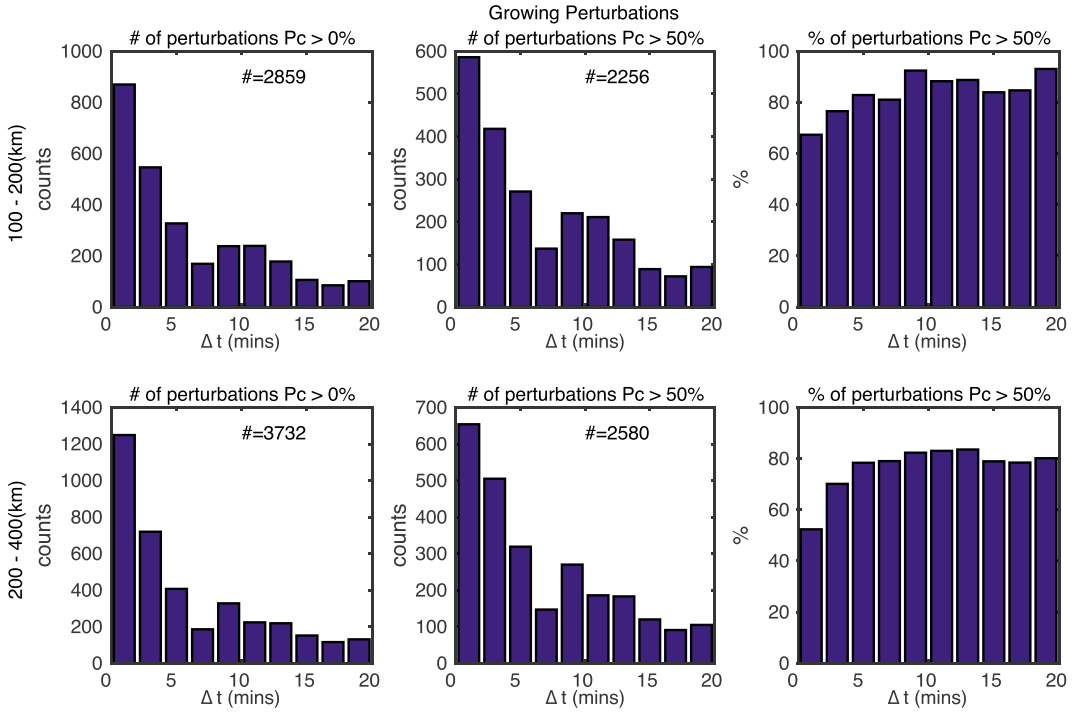

Figure 6. (left) The numbers of all growing perturbations, (middle) growing perturbations with more than 50% changes in magnitude, and (right) the percentage of the growing perturbations with more than 50% changes in magnitude as a function of time difference.

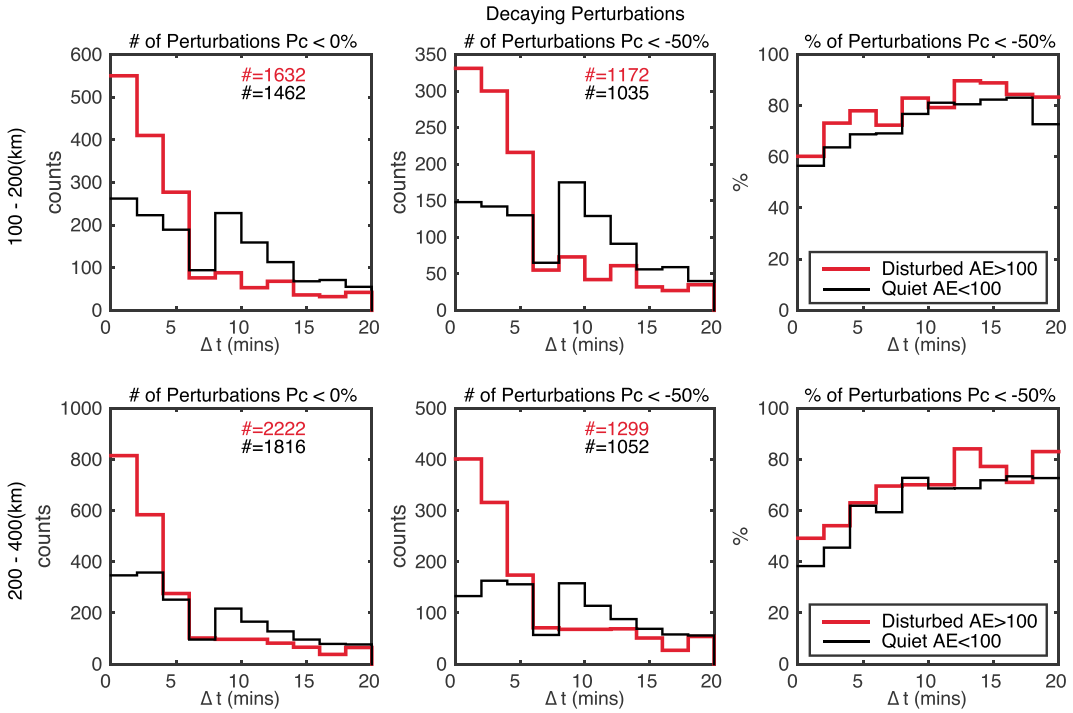

Figure 7. The format is same as Figure 5 for decaying perturbations during disturbed (red) and quiet time (black).

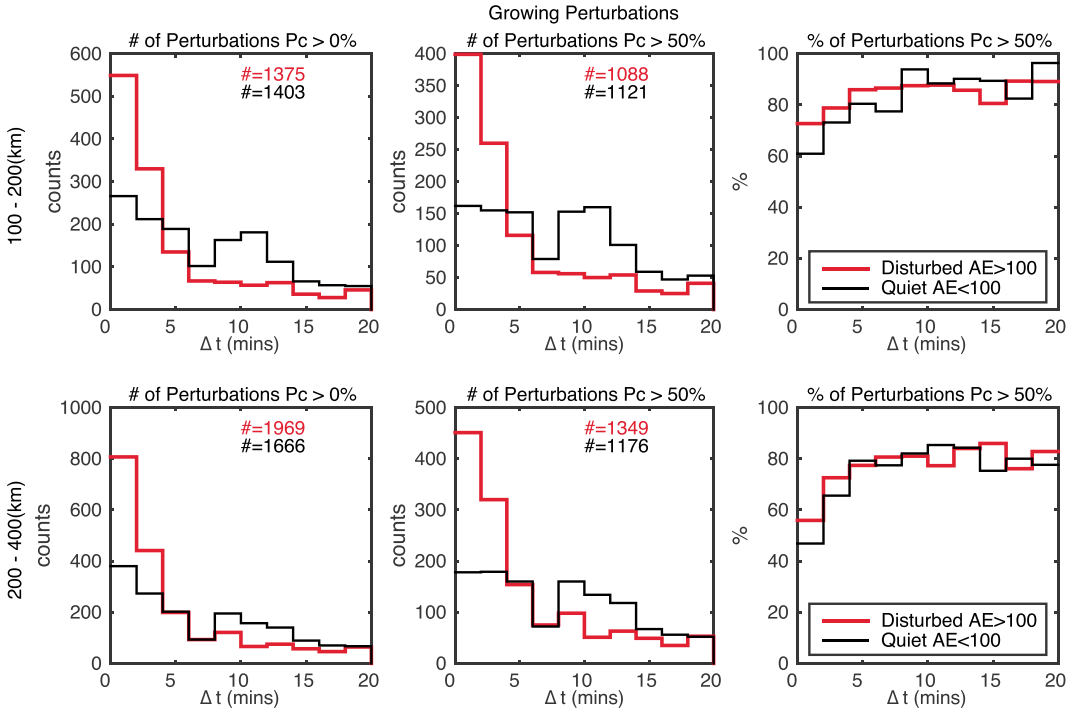

Figure 8. The format is same as Figure 6 for growing perturbations during disturbed (red) and quiet time (black).

magnitude is slightly shorter for disturbed times (~9 min) than for quiet time (~11 min). For larger spatial scale perturbations, the same separation time is also shorter for disturbed times (~13 min) than for quiet time (>20 min). In addition, within the first 5 min, there are more decaying perturbations that have decayed by a factor 2 for disturbed times than for quiet times. This is consistent with the shorter times at which flow perturbations are seen to grow by 80% during higher geomagnetic activity for all flow perturbations.

The dependence of growing flow perturbations on the magnetic activity is shown in Figure 8 in a similar format to Figure 7. For both smaller and larger scale perturbations, at the shortest time separations a slightly higher fraction of perturbations is seen in the right panels for disturbed times compared to quiet times. Smaller spatial scale perturbations take a slightly longer time to reach an 80% threshold during quiet time than during disturbed times, but within the first 2 min, the growth is quite rapid during both disturbed and quiet time. Larger scale perturbations are seen to grow more rapidly for disturbed time when observed with less than 5-min separation, but the separation times at which flow perturbations are seen to grow by 80% are almost the same for both disturbed and quiet conditions.

Note that we have also investigated the influence of IMF orientation for both growth and decay cases by examining the same histograms as Figures 7 and 8 during the periods of northward and southward IMF. Those histograms are found to be identical and suggesting that the temporal persistence of the mesoscale perturbations (100–400 km) does not depend on the direction of IMF B_z.

5. Discussions

In this study the temporal characteristics of mesoscale (100–400 km) plasma flow perturbations in the high-latitude ionosphere are described by characteristic times derived from the separation between consecutive samples in nearly the same volume. We have used the observed change in the magnitude of a flow perturbation by more than 50% to designate the total emergence or extinction of an event. With this definition, we specify a rise time and saturation time for growth and decay as those times at which 60% and 80% of flow perturbations observed either emerge or are extinguished. Using observations from two consecutive passes of DMSP satellites at almost constant altitude, we find rise times for decaying perturbation within a given volume of order 2 and 5 min, respectively, and saturation times of order 10 and 20 min, respectively, for

smaller spatial scales (100–200 km) and larger spatial scales (200–400 km). Corresponding rise times for growing perturbation for the same scale sizes are significantly different, with rise times of less than 2 min and about 3 min, respectively, and saturation times of 5 min for both scale sizes.

Gjerloev et al. (2011) presented a statistical study of the spatial and temporal characteristics of FACs using two consecutive satellites from the ST5 satellite and have shown that highly correlated FAC signatures exist for time scales shorter than a few minutes for scale size less than 400 km and on time scales of a few to 10 min for larger scales (>400 km). Coherent structures in auroral particle precipitation on a time scale of 1.5 min for scale sizes larger than 100 km have been reported by Boudouridis and Spence (2007), and the stability of these coherent structures decreases as the scale size decreases. Both features in the current and particle precipitation show approximately the same temporal characteristic on order of a few minutes. It is not possible to directly compare our results with those previously reported since the analysis techniques and thresholds for detection are quite different. However, the same trend is evident with larger scale size perturbations being resident in a given volume for longer times than the smaller scale perturbations.

For observations made by satellites in almost the same orbit plane the observed time evolution may be due to temporal variations within a fixed volume or due to the motion of a spatially confined perturbation through the volume. If the flow perturbations grow and decay in place, then we find that their characteristic times for growth (1–5 min) are much shorter than the time for decay (2–20 min). Thus, the duration of a flow perturbation in a fixed volume is between 3 and 25 min. Over this period the flows imposed from the magnetosphere may additionally be influenced by changes in the effective impedance of the ionosphere (Matsuo & Richmond, 2008; Vickrey et al., 1986).

It is also possible that the difference in characteristic time for growth and decay is produced by motion of a fixed structure through the observed volume. In this case the apparently different characteristic times can be produced by different spatial distributions for the flows at the leading and trailing edges of the structure. Previous work by Chen and Heelis (2018) suggests that flow perturbations are embedded in the background flow with a median magnitude of 500 m/s. If perturbations move with the background flow, these perturbations can contribute to the large differences in characteristic times for growth and decay. Considering the saturation time for growth (~5 min) and decay (~20 min), the implied longitudinal dimensions for the leading and trailing edges would be up to 150 and 600 km, respectively, suggesting a local time extent for such convecting flow perturbations of about 750 km (~1.5 hr in local time).

Finally, a weak dependency on the geomagnetic activity is seen for both spatial scale sizes and for both growing and decaying flow perturbation, but almost no dependency on the IMF B_z is seen. Gjerloev et al. (2011) have shown that the temporal characteristic of FAC on the dayside is independent on IMF B_z and geomagnetic activity, but an increase in variability for disturbed condition is seen in the nightside. In our study, there are insufficient observations to separate dayside from nightside. However, more than 50% of the observations are in the dayside where we see only a weak dependency on AE and no dependency on IMF B_z. The work by Cousins et al. (2013) also found a weak correlation with AE index and almost no correlation with IMF B_z for smaller spatial (<1,000 km) and shorter temporal scale (a few tenth minutes) variability in the electric field.

6. Summary

Consecutive passes of DMSP spacecraft through the same ionospheric volume with time separations between a few seconds and 20 min have been used to examine the temporal characteristic of mesoscale plasma flow perturbations with latitudinal scale sizes of 100 to 200 km and 200 to 400 km. We find that within a fixed volume the rise times for growth (1–3 min) are shorter than the rise times for decay (2–5 min), and both are consistent with similar observations of FAC density and auroral emissions. Generally, both the rise and saturation times increase with increasing spatial scale sizes, but the saturation time for growth are about the same for different scale sizes. A weak dependence of rise times on the geomagnetic activity is seen for both spatial scale sizes and is also consistent with previous findings.

Previous observations of the flow perturbations (Chen & Heelis, 2018) show that they are quite uniformly distributed in local time and most frequently occupy the high-latitude extreme of the auroral oval and the

region just poleward of the convection reversal boundary. Since most perturbations are identified from latitudinal variations of the plasma velocity, the observations specify the latitudinal dimensions of the flow perturbations with high fidelity but restrict our knowledge of their longitudinal dimensions. It is possible that the mesoscale flow perturbations are local vortical flows with longitudinal and latitudinal dimensions that are comparable. Such flows most likely appear and disappear in a given volume on time scales between 3 and 25 min. Alternatively, and consistent with the longitude coherence of observed auroral emissions, it is possible that the mesoscale perturbations have longitudinal scale sizes of 750 km or more (>1 hr of local time) and move with the background flow.

Acknowledgments
This work is supported by AFOSR MURI grant FA9559-16-1-0364. The interplanetary magnetic field data are available via the Space Physics Data Facility OMNIWeb interface. The link to this database is http://omniweb.gsfc.nasa.gov. The DMSP ion drift data were obtained from the William B. Hanson Center for Space Sciences at the University of Texas at Dallas. The same data set is available at Madrigal CEDAR Database (cedar.openmadrigal.org). The authors thank Robin Coley, Marc Hairston, and Bob Power for its use.

References

Boudouridis, A., & Spence, H. E. (2007). Separation of spatial and temporal structure of auroral particle precipitation. *Journal of Geophysical Research*, *112*, A12217. https://doi.org/10.1029/2007JA012591

Chen, Y.-J., & Heelis, R. A. (2018). Mesoscale plasma convection perturbations in the high-latitude ionosphere. *Journal of Geophysical Research: Space Physics*, *123*. https://doi.org/10.1029/2018JA025716, 7609–7620.

Codrescu, M. V., Fuller-Rowell, T. J., & Foster, J. C. (1995). On the importance of E-field variability for Joule heating in the high-latitude thermosphere. *Geophysical Research Letters*, *22*(17), 2393–2396. https://doi.org/10.1029/95GL01909

Codrescu, M. V., Fuller-Rowell, T. J., Foster, J. C., Holt, J. M., & Cariglia, S. J. (2000). Electric field variability associated with the Millstone Hill electric field model. *Journal of Geophysical Research*, *105*(A3), 5265–5273. https://doi.org/10.1029/1999JA900463

Cousins, E. D. P., Matsuo, T., & Richmond, A. D. (2013). Mesoscale and large-scale variability in high-latitude ionospheric convection: Dominant modes and spatial/temporal coherence. *Journal of Geophysical Research: Space Physics*, *118*, 7895–7904. https://doi.org/10.1002/2013JA019319

Cousins, E. D. P., & Shepherd, S. G. (2010). A dynamical model of high-latitude convection derived from SuperDARN plasma drift measurements. *Journal of Geophysical Research*, *115*, A12329. https://doi.org/10.1029/2010JA016017

Cousins, E. D. P., & Shepherd, S. G. (2012). Statistical maps of small-scale electric field variability in the high-latitude ionosphere. *Journal of Geophysical Research*, *117*, A12304. https://doi.org/10.1029/2012JA017929

Deng, Y., Maute, A., Richmond, A. D., & Roble, R. G. (2009). Impact of electric field variability on Joule heating and thermospheric temperature and density. *Geophysical Research Letters*, *36*, L08105. https://doi.org/10.1029/2008GL036916

Fuller-Rowell, T. J., Rees, D., Quegan, S., Moett, R. J., Codrescu, M. V., & Millward, G. H. (1996). A coupled thermosphere-ionosphere model; CTIM. In R. W. Schunk (Ed.), *STEP handbook of ionospheric models* (pp. 217–238). Logan, UT: Utah State University.

Gjerloev, J. W., Ohtani, S., Iijima, T., Anderson, B., Slavin, J., & Le, G. (2011). Characteristics of the terrestrial field-aligned current system. *Annales de Geophysique*, *29*(10), 1713–1729. https://doi.org/10.5194/angeo-29-1713-2011

Hairston, M. R., & Heelis, R. A. (1990). Model of the high-latitude ionospheric convection pattern during southward interplanetary magnetic field using DE 2 data. *Journal of Geophysical Research*, *95*(A3), 2333–2343. https://doi.org/10.1029/JA095iA03p02333

Hairston, M. R., & Heelis, R. A. (1995). Response time of the polar ionospheric convection pattern to changes in the north-south direction of the IMF. *Geophysical Research Letters*, *22*(5), 631–634. https://doi.org/10.1029/94GL03385

Hedin, A. E. (1987). MSIS-86 thermospheric model. *Journal of Geophysical Research*, *92*(A5), 4649–4662. https://doi.org/10.1029/JA092iA05p04649

Heelis, R. A., & Coley, W. R. (1988). Global and local Joule heating effects seen by DE 2. *Journal of Geophysical Research*, *93*(A7), 7551–7557 . https://doi.org/10.1029/JA093iA07p07551

Heelis, R. A., Lowell, J. K., & Spiro, R. W. (1982). A model of the high-latitude convection pattern. *Journal of Geophysical Research*, *87*(A8), 6339–6345. https://doi.org/10.1029/JA087iA08p06339

Johnson, E. S., & Heelis, R. A. (2005). Characteristics of ion velocity structure at high latitudes during steady southward interplanetary magnetic field conditions. *Journal of Geophysical Research*, *110*, A12301. https://doi.org/10.1029/2005JA011130

Killeen, T. L., Hays, P. B., Carignan, G. R., Heelis, R. A., Hanson, W. B., Spencer, N. W., & Brace, L. H. (1984). Ion-neutral coupling in the high-latitude *F* region: Evaluation of ion heating terms from Dynamics Explorer 2. *Journal of Geophysical Research*, *89*(A9), 7495–7508. https://doi.org/10.1029/JA089iA09p07495

Matsuo, T., & Richmond, A. D. (2008). Effects of high-latitude ionospheric electric field variability on global thermospheric Joule heating and mechanical energy transfer rate. *Journal of Geophysical Research*, *113*, A07309. https://doi.org/10.1029/2007JA012993

Matsuo, T., Richmond, A. D., & Hensel, K. (2003). High-latitude ionospheric electric field variability and electric potential derived from DE-2 plasma drift measurements: Dependence on IMF and dipole tilt. *Journal of Geophysical Research*, *108*(A1), 1005. https://doi.org/10.1029/2002JA009429

Pettigrew, E. D., Shepherd, S. G., & Ruohoniemi, J. M. (2010). Climatological patterns of high-latitude convection in the northern and southern hemispheres: Dipole tilt dependencies and interhemispheric comparisons. *Journal of Geophysical Research*, *115*, A07305. https://doi.org/10.1029/2009JA014956

Rich, F. J., & Hairston, M. (1994). Large-scale convection patterns observed by DMSP. *Journal of Geophysical Research*, *99*(A3), 3827–3844. https://doi.org/10.1029/93JA03296

Ruohoniemi, J. M., & Greenwald, R. A. (1996). Statistical patterns of high-latitude convection obtained from Goose Bay HF radar observations. *Journal of Geophysical Research*, *101*(A10), 21,743–21,763. https://doi.org/10.1029/96JA01584

Ruohoniemi, J. M., & Greenwald, R. A. (2005). Dependencies of high-latitude plasma convection: Consideration of interplanetary magnetic field, seasonal, and universal time factors in statistical patterns. *Journal of Geophysical Research*, *110*, A09204. https://doi.org/10.1029/2004JA010815

St.-Maurice, J.-P., & Schunk, R. W. (1981). Ion-neutral momentum coupling near discrete high-latitude ionospheric features. *Journal of Geophysical Research*, *86*(A13), 11,299–11,321. https://doi.org/10.1029/JA086iA13p11299

Vasyliunas, V. M., & Song, P. (2005). Meaning of ionospheric Joule heating. *Journal of Geophysical Research*, *110*, A02301. https://doi.org/10.1029/2004JA010615

Vickrey, J. F., Livingston, R. C., Walter, N. B., Potemra, T. A., Heelis, R. A., Kelley, M. C., & Rich, F. J. (1986). On the current-voltage relationship of the magnetospheric generator at intermediate spatial scales. *Geophysical Research Letters*, *13*(6), 495–498. https://doi.org/10.1029/GL013i006p00495

Vickrey, J. F., Vondrak, R. R., & Matthews, S. J. (1982). Energy deposition by precipitating particles and Joule dissipation in the auroral ionosphere. *Journal of Geophysical Research*, *87*(A7), 5184–5196. https://doi.org/10.1029/JA087iA07p05184

Weimer, D. R. (2001). An improved model of ionospheric electric potentials including substorm perturbations and application to the Geospace Environment Modeling November 24, 1996, event. *Journal of Geophysical Research*, *106*(A1), 407–416. https://doi.org/10.1029/2000JA000604

Yu, Y., & Ridley, A. J. (2009). Response of the magnetosphere-ionosphere system to a sudden southward turning of interplanetary magnetic field. *Journal of Geophysical Research*, *114*, A03216. https://doi.org/10.1029/2008JA013292